TECHNISCHE MECHANIK, 32, 1, (2012), 3 – 20
submitted: October 27, 2011

Comparison of Two Bulk Energy Approaches for the Phasefield Modeling of Two-variant Martensitic Laminate Microstructure

F. E. Hildebrand, C. Miehe

The unusual thermomechanical properties of shape memory alloys are closely connected to the formation and evolution of their microstructure. At lower temperatures, shape memory alloys typically consists of martensitic laminates with coherent twin boundaries. We propose a large strain phasefield model for the formation and dissipative evolution of such two-variant martensitic twinned laminate microstructures. Our model accounts for the coherence-dependence of the interface energy density and contains a Ginzburg-Landau type evolution equation. We introduce two conceptually different modeling approaches for the regularized bulk energy, i.e. external and internal mixing. We construct a suitable gradient-extended incremental variational framework for the proposed formulation and discretize it by use of finte elements. Finally, we demonstrate the modeling capabilities of our formulation by means of two-dimensional finite element simulations of laminate formation in two-phasic martensitic CuAlNi and compare the energetic modeling properties of the two proposed bulk energy approaches.

1 Introduction

In this work, we present a large strain phasefield model for two-variant martensitic laminate microstructure. Our model accounts for the coherence-dependence of the surface energy of twin interfaces and employs an evolution of generalized Ginzburg-Landau type. We consider two different approaches to the modeling of bulk energy and compare their modeling capabilities by means of numerical examples.

Martensitic laminates in shape memory alloys such as NiTi or CuAlNi are microstructures that consist of different variants of the martensitic crystal phase. They form sharp, coherent interfaces – so called twin boundaries – whose motion is connected to displacive, diffusionless first-order solid to solid phase transformations. Generally, the behavior of the different variants can be considered elastic and reversible, whereas the phase boundary motion and hence the phase transformation is considered dissipative. See, e.g., James (1981), Bhattacharya (2003) and Abeyaratne and Knowles (2006), for an overview of crystallographic, energetic and kinetic aspects of shape memory materials.

Due to their extraordinary properties, shape memory alloys are used in a number of technical applications, see e.g. Duerig et al. (1990). A reliable modeling of the complex behavior of these materials is hence of great interest. A number of macroscale models have been proposed, see e.g. Bertram (1982), Boyd and Lagoudas (1996), Qidwai and Lagoudas (2000), Auricchio et al. (1997) or Helm and Haupt (2003). However, the predictive capabilities of these models are often limited. To substantially improve the macroscale models for martensitic transformations, a profound understanding of microstructural phenomena is indespensable. Such understanding can be gained by the use of mesoscale models that resolve and predict the evolving spatial morphology of the microstructure based on micromechanical modeling ingredients. Such ingredients are a coherence-dependent interface energy density, see Murr (1975) and Porter and Easterling (1992) or kinetic relations, see e.g. Hildebrand and Abeyaratne (2008) for related atomistic simulations and Faran and Shilo (2011) for related experimental observations.

Basis for such mesoscale models is the continuum-mechanical theory of sharp interfaces, see e.g. Abeyaratne and Knowles (1990, 2006). Depending on the chosen description of the sharp interface topology, mesoscopic continuum models for martensitic transformation fall into two categories: sharp interface approaches that model the interfaces as real discontinuity surfaces and regularized sharp interface approaches that make use of a smooth approximation of the discontinuities. Examples for sharp interface approaches are adaptive meshing strategies as employed by Merkle and Rohde (2006), the level-set method as desribed in Hou et al. (1999) and the extended finite element/level-set approach as used by Ji et al. (2002). All these approaches generally face great difficulties to

describe complex microstructure. This inherent difficulty can be overcome by the use of regularized sharp interface approaches which belong to the class of phasefield models. They are based on the approximation of the sharp discontinuities between different phases by smooth transitions of suitable order parameters. Such regularizations of the sharp interface theory are treated in a general continuum-thermodynamical context in Fried and Gurtin (1993) and Fried and Grach (1997), where the sharp interface topology as well as the surface energy of the interface are smeared out over a region proportional to a chosen regularization length scale. All such approaches go back to the classical Ginzburg-Landau equation as described in Allen and Cahn (1979) or Gurtin (1996). A relation between variational equilibrium phase field problems and the resulting variational sharp interface problems can be established by the use of Γ-convergence, see e.g. Modica (1987) and Alberti et al. (2005). For time-dependent evolution problems, a similar relation can be established by an asymptotic analysis, see e.g. Fried and Gurtin (1993) and Alber and Zhu (2008).

Extensive work on the phasefield modeling of martensitic transformations has been carried out in the past. E.g. Rasmussen et al. (2001) and Jacobs et al. (2003) use certain strain components as order parameters in a small strain context. Levitas et al. (2010) and Artemev et al. (2002) also use a small strain setting but employ the volume fractions of the different phases as order parameters. The main drawback of these approaches is the use of small strains in the context of a phasefield description of martensitic transformations. This causes two basic problems: (i) small strains are not suited to describe the relatively large rotations connected with the formation of twin interfaces and (ii) coherence-dependence can be properly modeled by the use of anisotropy only in the reference configuration in a large strain setting. An example for a large strain phasefield model is Levitas et al. (2009). However, this work is not a regularized sharp interface model in the meaning introduced here as it does not approximate sharp topologies by enforcing phase separation but allows for regions of phase mixture away from the interface.

In this work, we outline a phasefield model for the analysis of the formation and time-dependent evolution of martensitic laminate microstructure. We put a specific emphasis on the modeling of the regularized bulk energy, where we compare two different modeling approaches: The external mixing as employed, e.g., by Fried and Grach (1997) and an alternative internal mixing approach. We comment on advantages and drawbacks with respect to energetic conciseness and driving force modeling. The proposed regularized sharp interface approach is then shown to be capable of predicting the characteristic formation of twinned laminate microstructure in CuAlNi as observed experimentally, e.g., by Abeyaratne et al. (1996). Section 3 introduces the underlying sharp interface problem for a two-variant martensitic material. Section 4 explains the geometrically motivated approach to the regularized description of sharp topologies, allowing the statement of an analogous regularized problem in Section 5. Our models for the interface energy and two possible bulk energy approaches are treated in Section 6 and the dissipative evolution of the phasefield is considered in Section 7. The model is embedded in a suitable gradient-extended time-discrete incremental variational formulation in Section 8 and spatially discretized in Section 9. Finally, numerical results are presented in Section 10 that underline the importance of a coherence-dependent interface energy and show the advantages of one of the bulk energy approaches when requiring energetic conciseness.

2 Basic Properties of Martensitic CuAlNi

Shape memory alloys can consist of (at least) two different crystal structures: At high temperatures, they form the high symmetry austenite, and at lower temperatures (or under appropriate loading) crystallographically equivalent variants of the low symmetry martensite. Here, we consider the alloy CuAlNi that exhibits a cubic austenitic and an orthorhombic martensitic phase. Specifically, we will treat mixtures of two of the six orthorhombic martensitic variants of this shape memory alloy. These variants are characterized by the use of two Bain tensors that describe the martensitic variants as deformations with respect to the cubic austenitic reference configuration

$$\boldsymbol{U}_1 = \begin{bmatrix} \frac{\alpha+\gamma}{2} & \frac{\alpha-\gamma}{2} & 0 \\ \frac{\alpha-\gamma}{2} & \frac{\alpha+\gamma}{2} & 0 \\ 0 & 0 & \beta \end{bmatrix} \quad \text{and} \quad \boldsymbol{U}_2 = \begin{bmatrix} \frac{\alpha+\gamma}{2} & \frac{\gamma-\alpha}{2} & 0 \\ \frac{\gamma-\alpha}{2} & \frac{\alpha+\gamma}{2} & 0 \\ 0 & 0 & \beta \end{bmatrix}, \tag{1}$$

with parameters $\alpha = 1.0619$, $\beta = 0.9178$ and $\gamma = 1.0231$, see Ostsuka and Shimizu (1974). The stability of the martenistic variants implies that the individual free energies of the variants $\psi_1(\boldsymbol{F})$ and $\psi_2(\boldsymbol{F})$ have minima at $\boldsymbol{U}_1$ and $\boldsymbol{U}_2$, respectively, leading to the requirements

$$\psi_1(\boldsymbol{R}\boldsymbol{U}_1) \leq \psi_1(\boldsymbol{F})\ \forall \boldsymbol{R} \in SO(3),\ \forall \boldsymbol{F} \in \mathcal{R}^{3\times 3}_+ \quad \text{and} \quad \psi_2(\boldsymbol{R}\boldsymbol{U}_2) \leq \psi_2(\boldsymbol{F})\ \forall \boldsymbol{R} \in SO(3),\ \forall \boldsymbol{F} \in \mathcal{R}^{3\times 3}_+, \tag{2}$$

where $\mathcal{R}^{3\times 3}_+$ is the set of all second order tensors with positive determinant. Crystal symmetry relations further

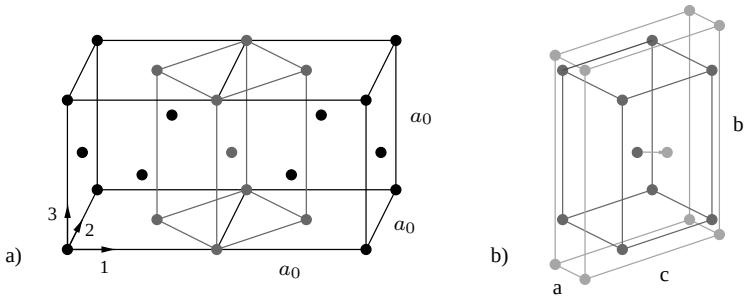

Figure 1: *The martensitic transformation of CuAlNi. a) The cubic austenite lattice (black) and b) one variant of the orthorhombic martensite lattice (light grey). The medium grey cell is shown in both cases for comparison.*

imply equal energy of the martenisitc variants

$$\psi_1(\boldsymbol{R}\boldsymbol{U}_1) = \psi_2(\tilde{\boldsymbol{R}}\boldsymbol{U}_2) \quad \forall \boldsymbol{R}, \tilde{\boldsymbol{R}} \in SO(3)\,. \tag{3}$$

In certain situations, this can lead to a coexistence of the variants, which then usually form a twinned laminate microstructure with coherent sharp interfaces. The two variants 1 and 2 can form such a kinematically compatible low energy interface if

$$\exists \boldsymbol{Q}, \boldsymbol{a}, \boldsymbol{m}_o \quad \text{s.t.} \quad \boldsymbol{Q}\boldsymbol{U}_1 - \boldsymbol{U}_2 = \boldsymbol{a} \otimes \boldsymbol{m}_o\,, \tag{4}$$

where $\boldsymbol{m}_o$ is the reference normal of the resulting (sharp) twin boundary. In other words, out of all reference interface normals $\boldsymbol{m}$, the normal $\boldsymbol{m}_o$ is the one that allows the connection of the two bulk-energy-minimizing deformation states $\boldsymbol{U}_1$ and $\boldsymbol{U}_2$ by a coherent and hence low energy interface. Equation (4) is referred to as the twinning equation and generally has two solutions, see Ball and James (1987). For $\boldsymbol{U}_1$ and $\boldsymbol{U}_2$ as specified in (1), the two solutions of (4) are

$$\boldsymbol{Q}^1 = \begin{bmatrix} \frac{2\alpha\gamma}{\alpha^2+\gamma^2} & \frac{\alpha^2-\gamma^2}{\alpha^2+\gamma^2} & 0 \\ -\frac{\alpha^2-\gamma^2}{\alpha^2+\gamma^2} & \frac{2\alpha\gamma}{\alpha^2+\gamma^2} & \\ 0 & 0 & 1 \end{bmatrix}, \quad \boldsymbol{a}^1 = -\frac{\alpha^2-\gamma^2}{\alpha^2+\gamma^2} \begin{bmatrix} \alpha-\gamma \\ \alpha+\gamma \\ 0 \end{bmatrix}, \quad \boldsymbol{m}_o^1 = \begin{bmatrix} 1 \\ 0 \\ 0 \end{bmatrix}, \tag{5}$$

$$\boldsymbol{Q}^2 = \begin{bmatrix} \frac{2\alpha\gamma}{\alpha^2+\gamma^2} & -\frac{\alpha^2-\gamma^2}{\alpha^2+\gamma^2} & 0 \\ \frac{\alpha^2-\gamma^2}{\alpha^2+\gamma^2} & \frac{2\alpha\gamma}{\alpha^2+\gamma^2} & \\ 0 & 0 & 1 \end{bmatrix}, \quad \boldsymbol{a}^2 = -\frac{\alpha^2-\gamma^2}{\alpha^2+\gamma^2} \begin{bmatrix} \alpha+\gamma \\ \alpha-\gamma \\ 0 \end{bmatrix}, \quad \boldsymbol{m}_o^2 = \begin{bmatrix} 0 \\ 1 \\ 0 \end{bmatrix}. \tag{6}$$

see, e.g., Abeyaratne et al. (1996). In the following, when it is not essential to specify the particular solution being used, we shall simply write $\boldsymbol{Q}$, $\boldsymbol{a}$ and $\boldsymbol{m}_o$.

3 Sharp Interface Boundary Value Problem

As a basis for our considerations, we briefly summarize the continuum mechanical description of sharp interfaces as in twinned martensitic laminates. We consider a body with reference configuration $\mathcal{B}$ containing the material points $\boldsymbol{X} \in \mathcal{B}$. $\mathcal{B}$ consists of two subdomains $\mathcal{B}_1$ and $\mathcal{B}_2$ occupied by variant 1 and variant 2, respectively. The two subdomains are separated by the sharp interface Γ with reference normal $\boldsymbol{m}$, such that $\mathcal{B}_1 \cup \Gamma \cup \mathcal{B}_2 = \mathcal{B}$ and

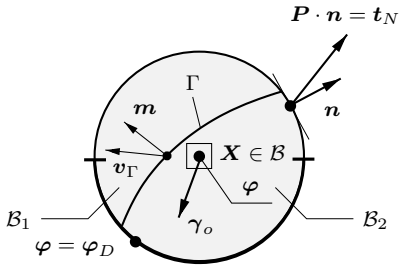

Figure 2: *Sharp interface formulation of the phase transformation problem in terms of the deformation map $\boldsymbol{\varphi}$.*

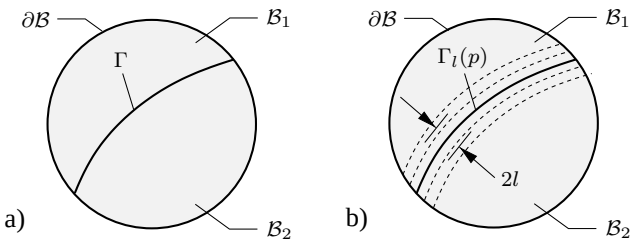

Figure 3: *Sharp and regularized interface topologies. a) The sharp interface surface* Γ *separates* $\mathcal{B}$ *into* $\mathcal{B}_1$ *and* $\mathcal{B}_2$*. b) The regularized surface* $\Gamma_l(p)$ *is a functional of the phasefield* p *and smears out* Γ *over* $2l$*.*

$\mathcal{B}_1 \cap \mathcal{B}_2 = \emptyset$. The deformation of the body is described by the deformation map $\boldsymbol{\varphi}$ that maps referential points $\boldsymbol{X}$ onto spatial points $\boldsymbol{\varphi}(\boldsymbol{X}) = \boldsymbol{x} \in \mathcal{S}$ that form the current configuration $\mathcal{S}$ of the body and by the deformation gradient $\boldsymbol{F} = \nabla\boldsymbol{\varphi}$. Furthermore, we assume that the body is subject to the referential body force $\boldsymbol{\gamma}$ and that the boundary $\partial\mathcal{B}$ can be decomposed into a Dirichlet part $\partial\mathcal{B}_{\boldsymbol{\varphi}}$, where the deformation is prescribed as $\boldsymbol{\varphi}_D$, and a von Neumann part $\partial\mathcal{B}_{\boldsymbol{t}} = \partial\mathcal{B} \setminus \partial\mathcal{B}_{\boldsymbol{\varphi}}$ where a traction is prescribed as $\boldsymbol{t}_N$, see Figure 2. Assuming quasistatic loading (such that the rate of phase transformation is much larger than the rate of loading) and isothermal conditions, we can write down the resulting sharp interface boundary value problem for a given interface Γ as

$$\operatorname{Div}\big(\partial_{\boldsymbol{F}}\psi_1\big) + \boldsymbol{\gamma} = \boldsymbol{0} \quad \text{in } \mathcal{B}_1 \tag{7}$$

$$\operatorname{Div}\big(\partial_{\boldsymbol{F}}\psi_2\big) + \boldsymbol{\gamma} = \boldsymbol{0} \quad \text{in } \mathcal{B}_2 \tag{8}$$

$$\partial_{\boldsymbol{F}}\psi_1 \cdot \boldsymbol{n} - \boldsymbol{t}_N = \boldsymbol{0} \quad \text{on } \partial\mathcal{B}_{\boldsymbol{t}} \cap \partial\mathcal{B}_1 \tag{9}$$

$$\partial_{\boldsymbol{F}}\psi_2 \cdot \boldsymbol{n} - \boldsymbol{t}_N = \boldsymbol{0} \quad \text{on } \partial\mathcal{B}_{\boldsymbol{t}} \cap \partial\mathcal{B}_2 \tag{10}$$

$$\boldsymbol{\varphi} - \boldsymbol{\varphi}_D = \boldsymbol{0} \quad \text{on } \partial\mathcal{B}_{\boldsymbol{\varphi}} \tag{11}$$

$$[\![\boldsymbol{F}]\!] \cdot \boldsymbol{s} = \boldsymbol{0} \quad \text{on } \Gamma\,, \forall \boldsymbol{s} \perp \boldsymbol{m} \tag{12}$$

where $[\![\cdot]\!]$ is the jump across the interface and where we have assumed that the two variants are hyperelastic materials with constitutive relations for the first Piola-Kirchhoff stress of the form $\boldsymbol{P}_1 = \partial_{\boldsymbol{F}}\psi_1$ and $\boldsymbol{P}_2 = \partial_{\boldsymbol{F}}\psi_2$ that require the constitutive prescription of the free energy density functions $\psi_1(\boldsymbol{F})$ and $\psi_2(\boldsymbol{F})$. Note that alternatively, one can also prescribe a single energy $\psi(\boldsymbol{F})$ with two wells corresponding to the minima $\boldsymbol{U}_1$ and $\boldsymbol{U}_2$.

If we further assume that the body is capable of undergoing phase transformations between variant 1 and 2 such that Γ can change its position in the reference configuration where $\boldsymbol{v}_\Gamma(\boldsymbol{X})$ denotes the referential interface propagation velocity, then we also have to prescribe a kinetic relation of the form

$$V = V(f_\Gamma)\,, \quad V = \boldsymbol{v}_\Gamma \cdot \boldsymbol{m}\,, \tag{13}$$

where f_Γ is the sharp interface driving force defined in terms of the jump operator $[\![\cdot]\!]$ by

$$f_\Gamma = \boldsymbol{m} \cdot [\![\psi\boldsymbol{1} - (\partial_{\boldsymbol{F}}\psi)^T\,\boldsymbol{F}]\!] \cdot \boldsymbol{m} - 2g_\Gamma\kappa_m\,, \tag{14}$$

where g_Γ is the constant interface energy density per unit area and κ_m is the mean curvature of the interface. Note that the quantity inside the jump brackets is the energy momentum tensor introduced by Eshelby (1956). For a more general treatment of the driving force also for the non-isothermal case (but without interface energy), see, e.g., Abeyaratne and Knowles (1990). Note that both the description of the time-dependent topology of Γ as well as the enforcement of the jump condition (12) can be very demanding in numerical simulations.

4 Smooth Phasefield Approximation of Sharp Interfaces

To circumvent the direct and often very complex description of the sharp interface Γ that separates the constituents of the martensitic laminate, we approximate its topology by use of a smooth *phasefield* $p(\mathbf{X}) \in [0, 1]$, see Figure 3, and thereby conceptually follow a recent work on regularized fracture, see Miehe et al. (2010). We associate $p = 0$ with variant 1 and $p = 1$ with variant 2. Assuming we are given a plane sharp interface with normal $\boldsymbol{m}$ that passes through the origin, we can use the function

$$p(\boldsymbol{X}) = \frac{1}{2}\left[\tanh\left(\frac{\boldsymbol{X}\cdot\boldsymbol{m}}{l}\right) + 1\right] \tag{15}$$

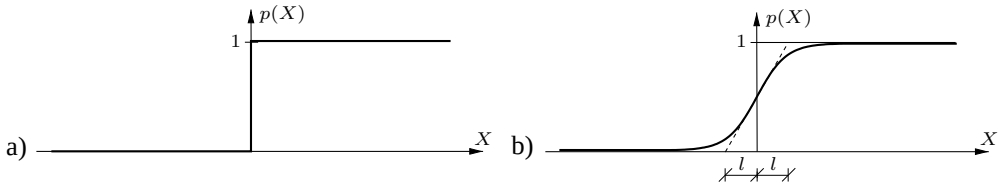

Figure 4: *Sharp and regularized interface modeling by use of an order parameter p: a) A sharp interface at $X = 0$ leads to a jump in $p(X)$. b) The interface can be regularized by introduction of a regularization length scale l.*

to smear out this sharp interface over the length $2l$, see Figure 4. Note that functions of the type (15) are solutions of the elliptic partial differential equation

$$l^2 \Delta p - 4\, p\,(1-p)\,(1-2p) = 0\,, \tag{16}$$

under appropriate boundary conditions. We can further state a related variational principle as the weak form of (16), namely

$$p(\boldsymbol{X}) = \arg \left\{ \inf_{p \,\in\, W} \Gamma_l(p) \right\}\,, \tag{17}$$

where the interface surface functional $\Gamma_l(p)$ is defined in terms of the interface surface density $\gamma_l(p, \nabla p)$ by

$$\Gamma_l(p) = \int_{\mathcal{B}} \gamma_l(p, \nabla p)\, dV \quad \text{with} \quad \gamma_l(p, \nabla p) = \frac{6}{l} p^2 (1-p)^2 + \frac{3l}{2} |\nabla p|^2\,. \tag{18}$$

Again, solutions of the type (15) will be the solutions of (17) under appropriate boundary conditions. The functional $\Gamma_l(p)$ as defined in (18) has the very nice property that it approximates the interface surface area $\mathrm{Surf}(\Gamma)$ in the limit of $l \to 0$, i.e.

$$\inf_{p \in W} \left\{ \lim_{l \to 0} \Gamma_l(p) \right\} = \mathrm{Surf}(\Gamma)\,, \tag{19}$$

see, e.g., Alberti et al. (2005) for a related consideration employing Γ-convergence.

5 Smooth Interface Boundary Value Problem

Having introduced the order parameter p, we can restate the sharp interface boundary value problem. Assuming we are given a sufficiently smooth function $p(\boldsymbol{X})$ that approximates the given sharp interface Γ as outlined in Section 4, we can write

$$\mathrm{Div}\big(\partial_{\boldsymbol{F}} \psi\big) + \boldsymbol{\gamma} = \boldsymbol{0} \quad \text{in } \mathcal{B}\,, \tag{20}$$

$$\partial_{\boldsymbol{F}} \psi \cdot \boldsymbol{n} - \boldsymbol{t}_N = \boldsymbol{0} \quad \text{on } \partial\mathcal{B}_{\boldsymbol{t}}\,, \tag{21}$$

$$\boldsymbol{\varphi} - \boldsymbol{\varphi}_D = \boldsymbol{0} \quad \text{on } \partial\mathcal{B}_{\boldsymbol{\varphi}}\,, \tag{22}$$

where we have again assumed a hyperelastic material with a constitutive relation of the form $\boldsymbol{P} = \partial_{\boldsymbol{F}} \psi$ that requires the constitutive prescription of an energy $\psi(\boldsymbol{F}, p, \nabla p)$ accounting both for bulk and interface effects that recovers $\boldsymbol{P}_1 = \partial_{\boldsymbol{F}} \psi$ for $p = 0$ and $\boldsymbol{P}_2 = \partial_{\boldsymbol{F}} \psi$ for $p = 1$.

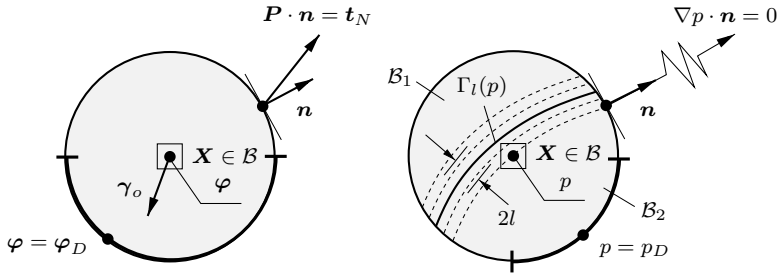

Figure 5: *Regularized interface formulation of the problem in terms of the deformation map $\boldsymbol{\varphi}$ and the phasefield p.*

If we further assume that the body is capable of undergoing phase transformations between variants 1 and 2, then we also have to prescribe a suitable evolution equation for p, leading to the initial boundary value problem

$$\dot{p} - \dot{p}(f) = 0 \quad \text{in } \mathcal{B}\,, \tag{23}$$
$$p(t=0) - p_0 = 0 \quad \text{in } \mathcal{B}\,, \tag{24}$$
$$\partial_{\nabla p}\psi \cdot \boldsymbol{n} = 0 \quad \text{on } \partial\mathcal{B} \setminus \partial\mathcal{B}_p\,, \tag{25}$$
$$p - p_D = 0 \quad \text{on } \partial\mathcal{B}_p\,, \tag{26}$$

where $\mathcal{B}_p$ is the phasefield Dirichlet boundary and where f is the smooth interface driving force usually defined as $f = -\delta\psi(\boldsymbol{F}, p, \nabla p)$, see section 7. Note that the introduction of the phasefield p has simplified the structure of the problem by removing the discontinuities at the cost of an additional field for the approximate description of the sharp topologies.

6 Energy Storage

The energy storage in martensitic laminates consists of two basic contributions: *interface energy* and *bulk energy*. The concise separation of these quantities is essential, e.g., for the prediction of size effects, where the two contributions compete. Inspired by, e.g., Fried and Grach (1997), we consequently model the stored energy functional Ψ as a sum of the interface energy functional Ψ_Γ and the bulk energy functional $\Psi_\mathcal{B}$. Specifically, we write

$$\Psi(p) = \Psi_\Gamma(p) + \Psi_\mathcal{B}(\boldsymbol{\varphi}, p)\,, \tag{27}$$

where the individual energy functionals are defined by

$$\Psi(\boldsymbol{\varphi}, p) = \int_\mathcal{B} \psi(\boldsymbol{F}, p, \nabla p)\, dV\,, \quad \Psi_\mathcal{B}(\boldsymbol{\varphi}, p) = \int_\mathcal{B} \psi_\mathcal{B}(\boldsymbol{F}, p)\, dV\,, \quad \Psi_\Gamma(p) = \int_\mathcal{B} \psi_\Gamma(p, \nabla p)\, dV\,. \tag{28}$$

Localization leads to an additive split of the energy density functions

$$\psi(\boldsymbol{F}, p, \nabla p) = \psi_\mathcal{B}(\boldsymbol{F}, p) + \psi_\Gamma(p, \nabla p)\,. \tag{29}$$

In the following, we will specify an interface energy density and propose two conceptually different approaches to the modeling of the mixed bulk energy.

6.1 Interface Energy

Starting from (18) and (19), the construction of a *coherence-independent* interface energy is straight forward. Introducing the interface energy density per unit area $g_\Gamma = \text{const.}$, we can immediately write

$$\Psi_\Gamma(p) = g_\Gamma\, \text{Surf}(\Gamma) \approx g_\Gamma\, \Gamma_l(p) \quad \Leftrightarrow \quad \int_\mathcal{B} \psi_\Gamma(p, \nabla p)\, dV = \int_\mathcal{B} g_\Gamma\, \gamma_l(p, \nabla p)\, dV\,. \tag{30}$$

From (30) we can identify the *coherence-independent* interface energy density as

$$\psi_\Gamma(p, \nabla p) = g_\Gamma\, \gamma_l(p, \nabla p) = g_\Gamma \left\{ \frac{6}{l} p^2 (1-p)^2 + \frac{3l}{2} |\nabla p|^2 \right\}\,. \tag{31}$$

As the interface energy in martensitic laminates is highly *coherence-dependent*, i.e. as the interface energy is much lower for coherent than for incoherent interfaces, see Murr (1975) and Porter and Easterling (1992), we now modify (31) suitably in order to energetically punish incoherent interfaces. Conceptually following Fried and Grach (1997), we suggest a *coherence-dependent* interface energy density of the form

$$\psi_\Gamma(p, \nabla p) = \hat{g}_\Gamma \left\{ \frac{6}{l}\, p^2 (1-p)^2 + \frac{3l}{2}\, \nabla p \left[\boldsymbol{1} + \lambda\, (\boldsymbol{1} - \boldsymbol{m}_o \otimes \boldsymbol{m}_o) \right] \nabla p \right\}\,, \tag{32}$$

where for $\lambda > 0$, deviations of the interface normal $\boldsymbol{m} = \nabla p / |\nabla p|$ from the coherent normal $\boldsymbol{m}_o$ defined in (4) are energetically punished, and where $\hat{g}_\Gamma$ is the interface energy density per unit area of a coherent interface.

6.2 Pure Phase Bulk Energies

As a starting point for the two presented approaches to the constitutive modeling of the regularized mixed bulk energy density $\psi_{\mathcal{B}}(\boldsymbol{F}, p)$, we first specify the bulk energy densities of the pure variants $\psi_1(\boldsymbol{F})$ and $\psi_2(\boldsymbol{F})$ as introduced in Section 4. A simple approach that satisfies the constraints (2) and (3) is to use an isotropic (poly-convex) free energy density function with a single well at $\boldsymbol{F} = \boldsymbol{1}$ and to shift its minimum to $\boldsymbol{R}\boldsymbol{U}_1$ and $\tilde{\boldsymbol{R}}\boldsymbol{U}_2$, $\boldsymbol{R}, \tilde{\boldsymbol{R}} \in SO(3)$, respectively. Here, we make use of the Neo-Hookean free energy function

$$\hat{\psi}(\boldsymbol{F}) = \frac{\hat{\mu}}{2}\big[\mathrm{tr}(\boldsymbol{F}^T\boldsymbol{F}) - 3\big] + \frac{\hat{\mu}}{\hat{\beta}}\big[\det(\boldsymbol{F})^{-\hat{\beta}} - 1\big]\,, \tag{33}$$

where $\hat{\mu}$ and $\hat{\beta}$ are material parameters. Shifting of the wells leads to the two bulk energy densities

$$\psi_1(\boldsymbol{F}) = \hat{\psi}(\boldsymbol{F}\boldsymbol{U}_1^{-1}\boldsymbol{R}^T) \quad \text{and} \quad \psi_2(\boldsymbol{F}) = \hat{\psi}(\boldsymbol{F}\boldsymbol{U}_2^{-1}\tilde{\boldsymbol{R}}^T)\,, \quad \boldsymbol{R}, \tilde{\boldsymbol{R}} \in SO(3)\,. \tag{34}$$

Note that the shifts of the isotropic function $\hat{\psi}(\boldsymbol{F})$ by $\boldsymbol{R}\boldsymbol{U}_1$ and $\tilde{\boldsymbol{R}}\boldsymbol{U}_2$ induce an anisotropy in $\psi_1(\boldsymbol{F})$ and $\psi_2(\boldsymbol{F})$ that is consistent with the crystal symmetry of the variants. Because of our association of $p = 0$ with variant 1 and of $p = 1$ with variant 2, we now have to ensure that $\psi_{\mathcal{B}}(\boldsymbol{F}, p)$ fulfills the requirements

$$\begin{aligned}
&\psi_{\mathcal{B}}(\boldsymbol{F}, p=0) = \psi_1(\boldsymbol{F}) \quad &\Rightarrow \quad &\psi_{\mathcal{B}}(\boldsymbol{F}, p=0) = \hat{\psi}(\boldsymbol{F}\boldsymbol{U}_1^{-1}\boldsymbol{R}^T)\,, \quad \boldsymbol{R} \in SO(3)\,,\\
&\psi_{\mathcal{B}}(\boldsymbol{F}, p=1) = \psi_2(\boldsymbol{F}) \quad &\Rightarrow \quad &\psi_{\mathcal{B}}(\boldsymbol{F}, p=1) = \hat{\psi}(\boldsymbol{F}\boldsymbol{U}_2^{-1}\tilde{\boldsymbol{R}}^T)\,, \quad \tilde{\boldsymbol{R}} \in SO(3)
\end{aligned} \tag{35}$$

We will now consider two possible formulations that satisfy (35), and consider their further implications.

6.3 Externally Mixed Bulk Energy

One possible approach to the constitutive modeling of the regularized mixed bulk energy density is to mix the two free energies $\psi_1(\boldsymbol{F})$ and $\psi_2(\boldsymbol{F})$ *externally*, leading to

$$\psi^e_{\mathcal{B}}(\boldsymbol{F}, p) = (1 - h(p))\,\psi_1(\boldsymbol{F}) + h(p)\,\psi_2(\boldsymbol{F})\,, \tag{36}$$

where $h(p)$ is a ramping function with the properties $h(p = 0) = 0$ and $h(p = 1) = 1$ (and possibly $h'(p = 0) = h'(p = 1) = 0$), see, e.g., Fried and Grach (1997). With the simple and intuitive choice of $h(p) = p$ we obtain the regularized *externally mixed* bulk energy density $\psi^e_{\mathcal{B}}(\boldsymbol{F}, p)$ as

$$\psi^e_{\mathcal{B}}(\boldsymbol{F}, p) = (1 - p)\,\psi_1(\boldsymbol{F}) + p\,\psi_2(\boldsymbol{F})\,. \tag{37}$$

We can also express this in terms of the Neo-Hookean free energy function $\hat{\psi}$

$$\psi^e_{\mathcal{B}}(\boldsymbol{F}, p) = (1 - p)\,\hat{\psi}(\boldsymbol{F}\boldsymbol{U}_1^{-1}) + p\,\hat{\psi}(\boldsymbol{F}\boldsymbol{U}_2^{-1})\,. \tag{38}$$

Note that $\psi^e_{\mathcal{B}}(\boldsymbol{F}, p)$ can become negative, even though $\hat{\psi}(\boldsymbol{F})$ is strictly positive. Insertion of $p = 0$ and $p = 1$ into (38) immediately yields (35) with $\boldsymbol{R} = \tilde{\boldsymbol{R}} = \boldsymbol{1}$.

6.4 Internally Mixed Bulk Energy

Another approach to the constitutive modeling of the regularized mixed bulk energy density is to mix the two free energy densities $\psi_1(\boldsymbol{F})$ and $\psi_2(\boldsymbol{F})$ *internally*, i.e. to write the mixed free energy density as

$$\psi^i_{\mathcal{B}}(\boldsymbol{F}, p) = \hat{\psi}\big(\boldsymbol{F}\bar{\boldsymbol{U}}^{-1}(p)\big) \tag{39}$$

and to parametrize $\bar{\boldsymbol{U}}(p)$ in such a manner that

$$\bar{\boldsymbol{U}}(p = 0) = \boldsymbol{R}\boldsymbol{U}_1 \quad \text{and} \quad \bar{\boldsymbol{U}}(p = 1) = \tilde{\boldsymbol{R}}\boldsymbol{U}_2 \quad \text{with} \quad \boldsymbol{R}, \tilde{\boldsymbol{R}} \in SO(3)\,. \tag{40}$$

Even though the straight forward choice of $\bar{\boldsymbol{U}}(p)$ would be

$$\bar{\boldsymbol{U}}(p) = (1 - p)\,\boldsymbol{U}_1 + p\,\boldsymbol{U}_2\,, \tag{41}$$

we choose a parametrization along the rank-one connection between $\boldsymbol{U}_1$ and $\boldsymbol{U}_2$, leading to

$$\bar{\boldsymbol{U}}(p) = (1-p)\,\boldsymbol{Q}\boldsymbol{U}_1 + p\,\boldsymbol{U}_2 = \boldsymbol{Q}\boldsymbol{U}_1 - p\,\boldsymbol{a}\otimes\boldsymbol{m}_o\,, \tag{42}$$

where $\boldsymbol{Q}$, $\boldsymbol{a}$ and $\boldsymbol{m}_o$ are solutions of the twinning equation (3). The choice (42) is motivated by the fact that interfaces connecting $\boldsymbol{U}_1$ and $\boldsymbol{U}_2$ constitute rank-one connections. With (42), we can write the regularized *internally mixed* bulk energy density $\psi^i_{\mathcal{B}}(\boldsymbol{F},p)$ in terms of the Neo-Hookean free energy density $\hat{\psi}$ as

$$\psi^i_{\mathcal{B}}(\boldsymbol{F},p) = \hat{\psi}\big(\boldsymbol{F}\,[(1-p)\,\boldsymbol{Q}\boldsymbol{U}_1 + p\,\boldsymbol{U}_2]^{-1}\big) = \hat{\psi}\big(\boldsymbol{F}\,[\boldsymbol{Q}\boldsymbol{U}_1 - p\,\boldsymbol{a}\otimes\boldsymbol{m}_o]^{-1}\big)\,. \tag{43}$$

Note that $\psi^i_{\mathcal{B}}(\boldsymbol{F},p)$ cannot become negative as $\hat{\psi}(\boldsymbol{F})$ is strictly positive. Insertion of $p=0$ and $p=1$ into (43) yields (35) with $\boldsymbol{R}=\boldsymbol{Q}$ and $\tilde{\boldsymbol{R}}=\boldsymbol{1}$.

7 Dissipative Phasefield Evolution

Having specified the interface and bulk contributions to the energy density $\psi(\boldsymbol{F},p,\nabla p)$, we can now move on to prescribe the evolution of our internal variable p. This evolution is subject to a thermodynamic constraint, namely the dissipation inequality.

7.1 Dissipation Inequality

Since $\psi(\boldsymbol{F},p,\nabla p)$ contains the gradient ∇p, we start by evaluating the global dissipation inequality

$$\mathcal{D} = \int_{\mathcal{B}} \delta\; dV = \int_{\mathcal{B}} \Big[\boldsymbol{P} : \dot{\boldsymbol{F}} - \dot{\psi}(\boldsymbol{F},p,\nabla p)\Big]\; dV \geq 0\,. \tag{44}$$

and (obtaining the relation $\boldsymbol{P} = \partial_{\boldsymbol{F}}\psi$) reduce it to the local statement

$$\delta = -\,\delta_p\psi\;\dot{p} = -\,[\partial_p\psi - \mathrm{Div}\,(\partial_{\nabla p}\psi)]\;\dot{p} \geq 0\,, \tag{45}$$

where $\delta_p\psi$ is the variational or functional derivative of ψ with respect to p. Often, one introduces the driving force f and rewrites the dissipation inequality (45) as

$$\delta = f\;\dot{p} \geq 0 \quad \text{with} \quad f = -\,\delta_p\psi\,. \tag{46}$$

Equation (46) is the thermodynamic constraint on the evolution equation for p given by $\dot{p}(f)$.

7.2 Resulting Driving Forces

The additive decomposition of the energy density ψ into an interfacial part ψ_Γ and a bulk part $\psi_{\mathcal{B}}$ also allows an additive decomposition of the driving force f as defined in (46)

$$f = f_\Gamma + f_{\mathcal{B}}\,, \quad f_\Gamma = -\,\delta_p\psi_\Gamma\,, \quad f_{\mathcal{B}} = -\,\partial_p\psi_{\mathcal{B}}\,. \tag{47}$$

With the definition (32) of ψ_Γ, the interfacial part f_Γ of the driving force follows as

$$f_\Gamma\big(p,\nabla p\big) = \hat{g}_\Gamma\left[3l\;\mathrm{Div}\Big(\big[\boldsymbol{1} + \lambda\,(\boldsymbol{1}-\boldsymbol{m}_o\otimes\boldsymbol{m}_o)\,\big]\nabla p\Big) - \frac{12}{l}\;p\,(1-p)(1-2p)\right]. \tag{48}$$

For coherent interfaces with interface normals $\nabla p/|\nabla p| = \boldsymbol{m}_o$, equation (48) simplifies to

$$f_\Gamma\Big(p,\nabla p = |\nabla p|\boldsymbol{m}_o\Big) = \frac{3\hat{g}_\Gamma}{l}\left[l^2\;\Delta p - 4p\;(1-p)(1-2p)\right]. \tag{49}$$

Finally, from comparison of (49) with (16) we see that f_Γ as derived in (48) vanishes for $p(\boldsymbol{X})$ of the form (15) with coherent interface normal $\boldsymbol{m} = \boldsymbol{m}_o$, i.e.

$$p(\boldsymbol{X}) = \frac{1}{2}\left[\tanh\left(\frac{\boldsymbol{X}\cdot\boldsymbol{m}_o}{l}\right) + 1\right] \quad \Rightarrow \quad f_\Gamma\big(p,\nabla p\big) = 0\,. \tag{50}$$

We can hence interpret f_Γ as a driving force counteracting any deviations from the hyperbolic tangent shape and the coherent direction $\boldsymbol{m}_o$. Furthermore, the Laplacian Δp in f_Γ is related to the curvature part specified in (14).

Having analyzed the interface energy driving force f_Γ, we now turn to the evaluation and interpretation of the bulk energy driving force $f_\mathcal{B}$. Obviously, $f_\mathcal{B}$ depends on the choice of the bulk energy density $\psi_\mathcal{B}$, for which we have specified the two alternative definitions $\psi^e_\mathcal{B}$ and $\psi^i_\mathcal{B}$. The bulk energy driving force $f^e_\mathcal{B}$ resulting from the *externally mixed bulk energy density* $\psi^e_\mathcal{B}$ as given in (38) is

$$f^e_\mathcal{B}\big(\boldsymbol{F},p\big) = -\,\partial_p\psi^e_\mathcal{B}\big(\boldsymbol{F},p\big) = \hat\psi(\boldsymbol{F}\boldsymbol{U}_2^{-1}) - \hat\psi(\boldsymbol{F}\boldsymbol{U}_1^{-1}) = \psi_2(\boldsymbol{F}) - \psi_1(\boldsymbol{F}) = [\![\psi]\!]\,. \tag{51}$$

We thus observe that *external mixing* of the energies leads to a driving force proportional to the *energy jump* i.e. the energy part of the energy momentum tensor, see (14). The bulk energy driving force $f^i_\mathcal{B}$ resulting from the *internally mixed bulk energy density* $\psi^i_\mathcal{B}$ as defined in (39) is given by

$$f^i_\mathcal{B}\big(\boldsymbol{F},p\big) = -\,\delta_p\psi^i_\mathcal{B}\big(\boldsymbol{F},p\big) = -\partial_{\bar{\boldsymbol{U}}}\hat\psi\big(\boldsymbol{F}\bar{\boldsymbol{U}}^{-1}(p)\big) : \partial_p\big(\bar{\boldsymbol{U}}(p)\big)\,. \tag{52}$$

With the definition (42) of $\bar{\boldsymbol{U}}(p)$, equation (52) can be simplified to

$$f^i_\mathcal{B}\big(\boldsymbol{F},p\big) = \boldsymbol{m}_o\big(\boldsymbol{P}^T\boldsymbol{F}\big)\bar{\boldsymbol{U}}^{-1}\boldsymbol{a}\,. \tag{53}$$

From (53) we observe that *internal mixing* of the energies leads to a driving force that is connected to the momentum part $\boldsymbol{P}^T\boldsymbol{F}$ of the energy momentum tensor, see (14). Note that in contrast to (14), both $\boldsymbol{P}$ and $\boldsymbol{F}$ undergo a smooth transition in the interface region and are hence dependent on p.

7.3 Evolution Equation and Dissipation Potential

To complete our phasefield modeling of martensitic laminate microstructure, we now have to prescribe an evolution equation $\dot p(f)$ that satisfies the thermodynamic constraint (46). The simplest possibility to do so is to prescribe a linear relation between $\dot p$ and f, i.e.

$$\dot p = \frac{1}{\eta}\,f \quad\Rightarrow\quad \delta = \dot p f = \frac{1}{\eta}\,f^2 \geq 0\,, \tag{54}$$

where $\eta > 0$ is a viscosity parameter. This simple viscous evolution equation is a generalized Ginzburg-Landau equation of the form

$$\dot p = -\delta_p\psi\,, \tag{55}$$

see e.g. Gurtin (1996). An alternative way of specifying the evolution equation of p is to introduce a dissipation potential $\phi(\dot p)$ and to demand

$$\partial_{\dot p}\phi = f \quad\Rightarrow\quad \delta = \dot p f = \partial_{\dot p}\phi\,\dot p \geq 0\,. \tag{56}$$

It is easily seen from (56) that evolution equations of this kind are generally thermodynamically compatible if $\phi(\dot p)$ is (i) convex in $\dot p$, (ii) zero at the origin and (iii) always non-negative. This includes also functions with non-differentiable points, for which the definition $\partial_{\dot p}\phi$ has to be generalized to subgradients and for which the evolution equation is rewritten as

$$\partial_{\dot p}\phi - f \in 0 \quad\Leftrightarrow\quad \delta_{\dot p}\phi + \delta_p\psi \in 0\,. \tag{57}$$

The Ginzburg-Landau evolution equation (54) can be easily expressed in the form of (57) by choosing

$$\phi(\dot p) = \frac{\eta}{2}\dot p^2\,. \tag{58}$$

Note that even though (54) and (57) together with (58) specify a linear relation between $\dot p$ and f, this does not induce a linear relation between the normal velocity V of a moving phase boundary and the driving force f.

8 Incremental Variational Framework

To express the proposed phasefield model in a variational framework, we employ a gradient-extended incremental variational formulation, as outlined in Miehe (2010). To this end we introduce a time-discrete potential functional Π^τ given by

$$\Pi^\tau(\boldsymbol{\varphi},p;\boldsymbol{\varphi}_n,p_n) = \int_\mathcal{B}\left[\pi^\tau(\boldsymbol{F},p,\nabla p) - \boldsymbol{\gamma}\cdot(\boldsymbol{\varphi}-\boldsymbol{\varphi}_n)\right]\,dV - \int_{\partial\mathcal{B}_t}\boldsymbol{t}_N\cdot(\boldsymbol{\varphi}-\boldsymbol{\varphi}_n)\,dA\,, \tag{59}$$

where we call π^τ the *incremental internal work density* which we define by

$$\pi^\tau(\boldsymbol{F}, p, \nabla p; \boldsymbol{F}_n, p_n, \nabla p_n) = \psi_{\mathcal{B}}(\boldsymbol{F}, p) + \psi_\Gamma(p, \nabla p) - \psi(\boldsymbol{F}_n, p_n, \nabla p_n) + \tau\phi\big(\left[p - p_n\right]/\tau\big)\,, \tag{60}$$

where $\tau = t_{n+1} - t_n$ is the finite step size and where all quantities without the subscript $_n$ denote quantities at t_{n+1}. $\boldsymbol{\varphi}$ and p at t_{n+1} are then determined by the incremental minimization principle

$$\{\boldsymbol{\varphi}, p\} = \arg\left\{\inf_{\boldsymbol{\varphi}, p \in \mathcal{W}} \Pi^\tau(\boldsymbol{\varphi}, p; \boldsymbol{\varphi}_n, p_n)\right\}\,, \tag{61}$$

where $\mathcal{W}$ is the set of admissible solutions

$$\mathcal{W} = \big\{\ \{\boldsymbol{\varphi}, p\} \mid \boldsymbol{\varphi} = \boldsymbol{\varphi}_D \text{ on } \partial\mathcal{B}_{\boldsymbol{\varphi}} \text{ and } p = p_D \text{ on } \partial\mathcal{B}_p\ \big\}\,. \tag{62}$$

With the choice (58) for the dissipation potential ϕ, the time-discrete Euler equations of (61) follow as

$$\mathrm{Div}\big(\partial_{\boldsymbol{F}}\psi\big) + \boldsymbol{\gamma} = \boldsymbol{0} \quad \text{in } \mathcal{B}\,, \tag{63}$$

$$\partial_{\boldsymbol{F}}\psi \cdot \boldsymbol{n} = \boldsymbol{t}_N \quad \text{on } \partial\mathcal{B}_{\boldsymbol{t}}\,, \tag{64}$$

$$\eta(p - p_n) + \big[\partial_p\psi - \mathrm{Div}\big(\partial_{\nabla p}\psi\big)\big] = 0 \quad \text{in } \mathcal{B}\,, \tag{65}$$

$$\partial_{\nabla p}\psi \cdot \boldsymbol{n} = \boldsymbol{0} \quad \text{on } \partial\mathcal{B} \setminus \partial\mathcal{B}_p\,. \tag{66}$$

We identify equation (63) as the balance of linear momentum for $\boldsymbol{\varphi}$ specified in (20), equation (64) as the Neumann traction boundary condition for $\boldsymbol{\varphi}$ specified in (21), equation (65) as the time-discrete implicit algorithmic version of the evolution equation of p specified in (23) and equation (66) as the Neumann (zero) boundary condition for p as specified in (25). Furthermore, we see that (62) ensures the Dirichlet conditions (22) and (26).

9 Finite Element Discretization

To numerically solve the smooth boundary value problem specified in Section 5, we spatially discretize the time-discrete weak form (59) by use of the finite element method. Here, we restrict ourselves to domains $\mathcal{B} \in \mathcal{R}^d = 2$ and consequently also $\boldsymbol{\varphi} \in \mathcal{R}^d = 2$. We approximate the domain $\mathcal{B}$ by the union of E^h finite elements $\mathcal{B}_e^h$ with N^h global nodes, where h denotes the typical mesh size

$$\mathcal{B} \approx \bigcup_{e=1}^{E^h} \mathcal{B}_e^h\,. \tag{67}$$

On an individual finite element e with n^e nodes, we approximate the deformation $\boldsymbol{\varphi}$ and the phasefield p by use of the shape functions $N_I^e(\boldsymbol{X})$ as

$$\boldsymbol{\varphi}^h(\boldsymbol{X}) = \sum_{I=1}^{n^e} \begin{bmatrix} N_I^e & 0 & 0 \\ 0 & N_I^e & 0 \end{bmatrix} \boldsymbol{d}_I^e = \boldsymbol{N}_{\boldsymbol{\varphi}}^e \boldsymbol{d}^e\,, \tag{68}$$

$$p^h(\boldsymbol{X}) = \sum_{I=1}^{n^e} \begin{bmatrix} 0 & 0 & N_I^e \end{bmatrix} \boldsymbol{d}_I^e = \boldsymbol{N}_p^e \boldsymbol{d}^e\,, \tag{69}$$

where $\boldsymbol{d}_I^e = [\varphi_1, \varphi_2, p]^T$ is the vector containing the $d+1$ degrees of freedom at node I in element e and $\boldsymbol{d}^e = \Big[\boldsymbol{d}_1^{e\,T}, ..., \boldsymbol{d}_{n^e}^{e\,T}\Big]^T$ contains the collection of all $n^e(d+1)$ degrees of freedoms of the n^e nodes of element e. Similarly, the deformation gradient $\boldsymbol{F}$ is approximated by

$$\boldsymbol{F}^h(\boldsymbol{X}) = \nabla\boldsymbol{\varphi}^h(\boldsymbol{X}) = \begin{bmatrix} \varphi_{1,1}^h \\ \varphi_{2,2}^h \\ \varphi_{1,2}^h \\ \varphi_{2,1}^h \end{bmatrix} = \sum_{I=1}^{n^e} \begin{bmatrix} N_{I,1}^e & 0 & 0 \\ 0 & N_{I,2}^e & 0 \\ N_{I,2}^e & 0 & 0 \\ 0 & N_{I,1}^e & 0 \end{bmatrix} \boldsymbol{d}_I^e = \boldsymbol{B}_{\boldsymbol{\varphi}}^e \boldsymbol{d}^e\,, \tag{70}$$

and the approximation of the phasefield gradient ∇p follows as

$$\nabla p^h(\boldsymbol{X}) = \begin{bmatrix} p_{,1}^h \\ p_{,2}^h \end{bmatrix} = \sum_{I=1}^{n^e} \begin{bmatrix} 0 & 0 & N_{I,1}^e \\ 0 & 0 & N_{I,2}^e \end{bmatrix} \boldsymbol{d}_I^e = \boldsymbol{B}_p^e \boldsymbol{d}^e\,. \tag{71}$$

Finally, we relate the E^h element vectors $\boldsymbol{d}^e$ to the vector $\boldsymbol{d}$ containing the $N^h(d+1)$ global degrees of freedom by use of the finite element topology matrix $\boldsymbol{A}^e$

$$\boldsymbol{d}^e = \boldsymbol{A}^e \boldsymbol{d}\,. \tag{72}$$

We can now express $\boldsymbol{\varphi}$, p, $\boldsymbol{F}$ and ∇p in terms of $\boldsymbol{d}$ and hence rewrite the time-discrete potential $\Pi^\tau(\boldsymbol{\varphi}, p; \boldsymbol{\varphi}_n, p_n)$ in a time-space discrete form as $\Pi^h(\boldsymbol{d}; \boldsymbol{d}_n)$. This allows us to restate the time-discrete variational principle (61) in time-space-discrete form, i.e.

$$\boldsymbol{d} = \arg\left\{ \inf_{\boldsymbol{d}} \; \Pi^h(\boldsymbol{d}; \boldsymbol{d}_n) \right\}\,, \tag{73}$$

where $\boldsymbol{d}_n$ is the solution at time step t_n. Equation (73) can be solved by use of a Newton-Raphson type iteration leading to the update equation

$$\boldsymbol{d} \Leftarrow \boldsymbol{d} - [\,\Pi^h_{,\boldsymbol{dd}}\,]^{-1}[\Pi^h_{,\boldsymbol{d}}]\,. \tag{74}$$

Here we use bilinear quadrilateral finite elements for the discretization of both deformation $\boldsymbol{\varphi}$ and phasefield p.

10 Numerical Results

In this Section, we demonstrate the capability of our phasefield model to predict the formation of martensitic laminate microstructure in two dimensions by means of finite element simulations. Specifically, we analyze the influence of the incoherence-dependence and the choice of the bulk energy on the formation of microstructure. Finally, we investigate the energetics of laminates with increasing fineness.

10.1 Boundary Value Problem

All subsequent simulations are based on the following boundary value problem: Given is a body $\mathcal{B}$ consisting of the two orthorhombic martensitic variants 1 and 2 of CuAlNi. The Bain tensors of the two variants are given by $\boldsymbol{U}_1$ and $\boldsymbol{U}_2$, see (1). Recalling equation (2) we know that $\boldsymbol{U}_1$ and $\boldsymbol{U}_2$ can form kinematically compatible twin interfaces, i.e. there exist $\boldsymbol{Q}$, $\boldsymbol{a}$ and $\boldsymbol{m}_o$ such that

$$\boldsymbol{Q}\boldsymbol{U}_1 - \boldsymbol{U}_2 = \boldsymbol{a} \otimes \boldsymbol{m}_o\,. \tag{75}$$

The boundary of the body $\partial\mathcal{B}$ is now deformed by

$$\boldsymbol{\varphi}(\boldsymbol{X}) = \boldsymbol{F}_\xi \boldsymbol{X} \quad \text{on} \quad \partial\mathcal{B}, \quad \boldsymbol{F}_\xi = (1-\xi)\boldsymbol{Q}\boldsymbol{U}_1 + \xi \boldsymbol{U}_2, \quad \xi \in [0,1]\,, \tag{76}$$

i.e. by a deformation gradient lying on the rank-one connection between $\boldsymbol{Q}\boldsymbol{U}_1$ and $\boldsymbol{U}_2$. Chipot and Kinderlehrer (1988) have shown that under the assumption that coherent interfaces have no interface energy, the described boundary value problem is solved by an infinitely fine laminate of variants 1 and 2 with twin boundary normals $\boldsymbol{m}_o$ satisfying (2) and with volume fractions $1-\xi$ and ξ, respectively, see Figure 6.

To solve a boundary value problem of the presented kind for a material with coherence-dependent interface energy, we specify the domain

$$\mathcal{B} = \{\boldsymbol{X} \mid \boldsymbol{X} \in [0, L] \times [0, H]\}\,, \tag{77}$$

where $L = 1.0 \times 10^{-7}$m and $H = 5.0 \times 10^{-8}$m and apply the boundary conditions specified in (76) with $\xi = 1/2$. We discretize this domain by 400×200 bilinear quadrilateral elements, leading to a mesh size of $h \approx 2.5 \times 10^{-10}$m.

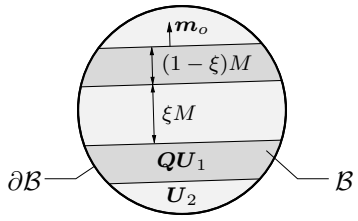

Figure 6: *A boundary value problem of the type considered by Chipot and Kinderlehrer (1988): The boundary $\partial\mathcal{B}$ of a domain $\mathcal{B}$ is deformed by $\boldsymbol{\varphi}(\boldsymbol{X}) = \boldsymbol{F}_\xi \boldsymbol{X}$ where $\boldsymbol{F}_\xi$ lies on the rank-one connection between $\boldsymbol{Q}\boldsymbol{U}_1$ and $\boldsymbol{U}_2$. In the absence of interface energy, analytical solutions are given by infinitely fine laminates of $\boldsymbol{Q}\boldsymbol{U}_1$ and $\boldsymbol{U}_2$ with volume fractions ξ and $(1-\xi)$ and laminate thickness M.*

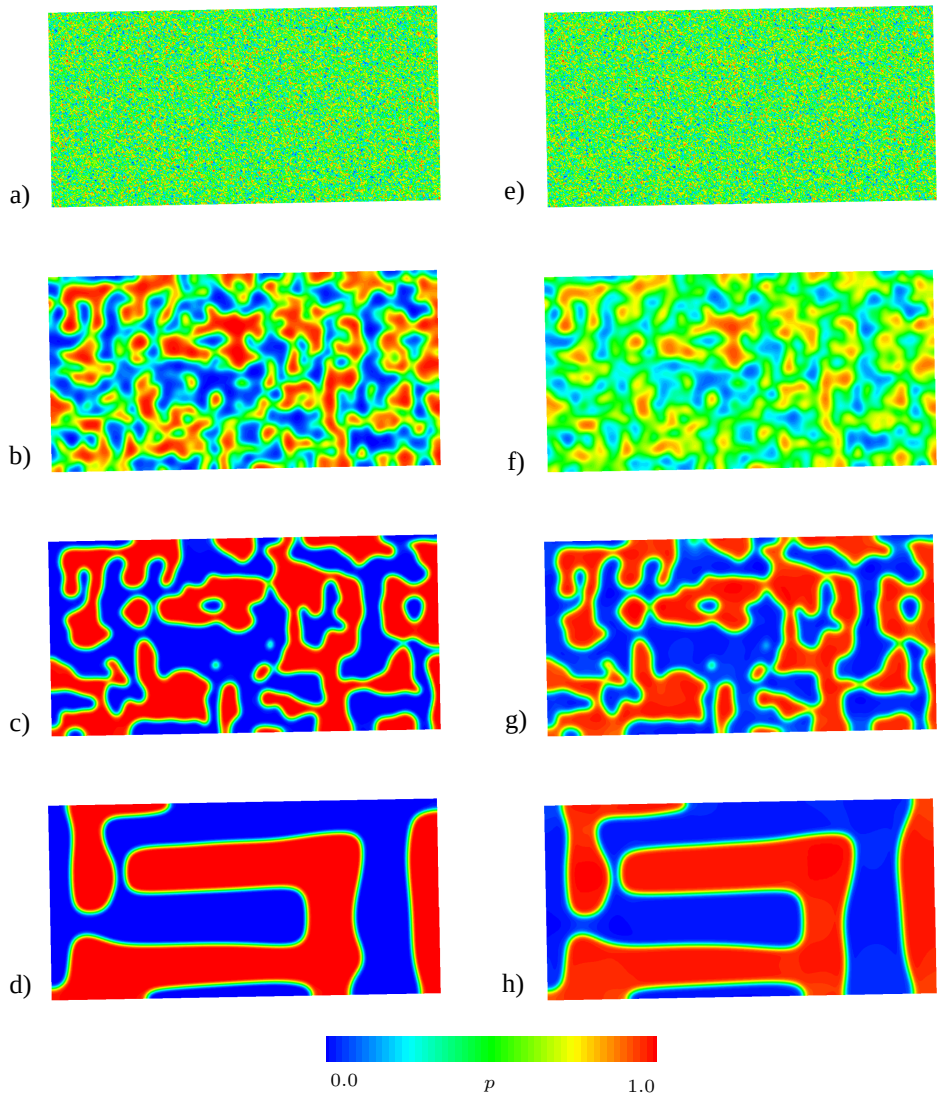

Figure 7: *Evolution of an initially random phasefield distribution $p(\boldsymbol{x})$ in a domain under boundary conditions (76) for a* ***coherence-independent*** *interface energy density ψ_Γ ($\lambda = 0$). a) – d) show snapshots of the evolution for an* ***externally mixed*** *bulk energy density $\psi^e_\mathcal{B}$, whereas e) – h) illustrate the evolution for the* ***internally mixed*** *bulk energy density $\psi^i_\mathcal{B}$.*

10.2 Material Parameters

bulk shear modulus	$\hat{\mu}$	=	7.0×10^9 N/m^2
bulk exponent	$\hat{\beta}$	=	2.0
coherent interface energy density	$\hat{g}_\Gamma$	=	21.0 mJ/m^2
interface incoherence sensitivity	λ	=	0.0 / 1.0×10^2
viscosity	η	=	1.0×10^{-5} Nms
regularization length	l	=	7.5×10^{-10} m

Table 1: *Material Parameters for Martensitic CuAlNi*

Table 1 summarizes the material parameters used in the simulations. $\hat{\mu}$ and $\hat{\beta}$ are chosen to lie in a realistic range for copper. Note in this context that the effective stiffness at the martensitic wells is modified by the shift with $\boldsymbol{U}_1^{-1}$ and $\boldsymbol{U}_2^{-1}$. For the coherent twin interface energy density $\hat{g}_\Gamma$ we use the value given in Murr (1975) for the interface surface energy density of a coherent twin interface in copper, see also Porter and Easterling (1992). The associated incoherence penalty parameter $\lambda = 100.0$ is not based on any experimental data. Its influence on the

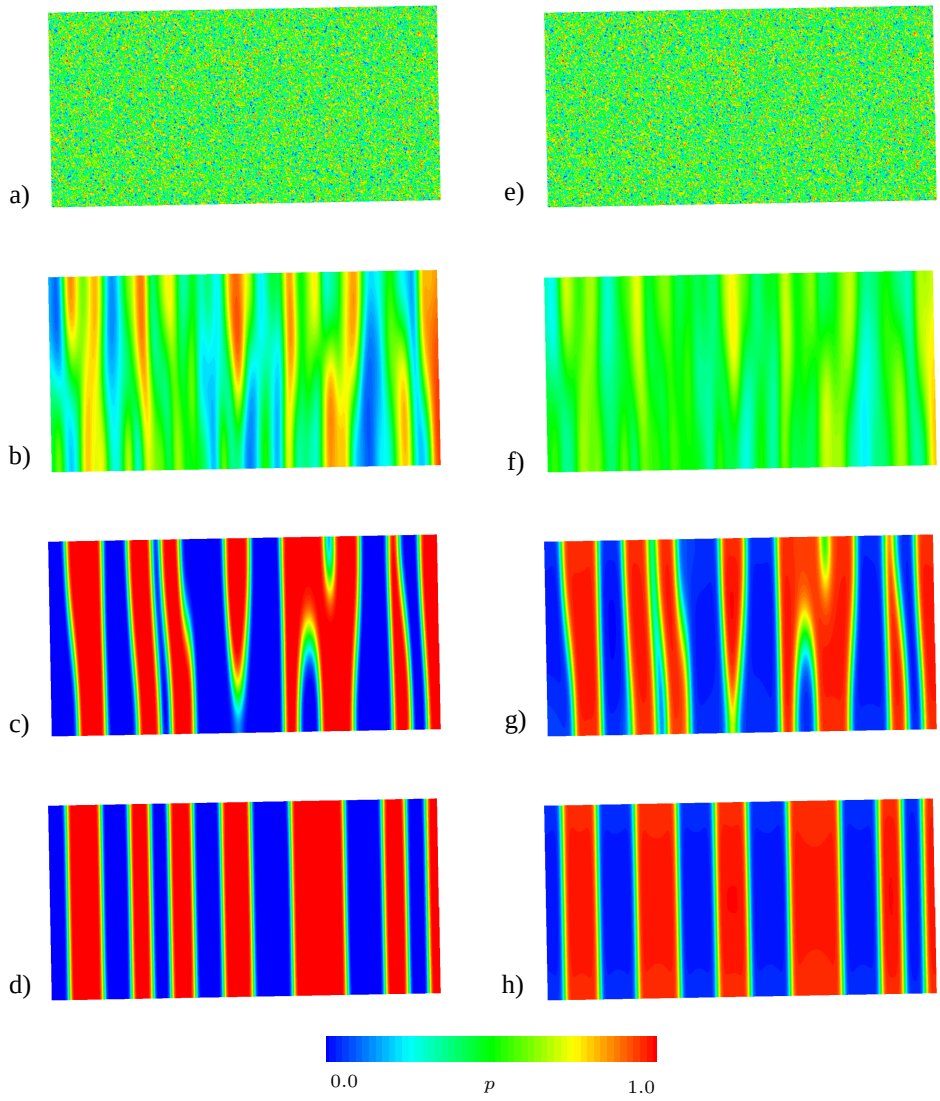

Figure 8: *Evolution of an initially random phasefield distribution $p(\boldsymbol{x})$ in a domain under boundary conditions (76) for a **coherence-dependent** interface energy density ψ_Γ ($\lambda = 100.0$). a) – d) show snapshots of the evolution for an **externally mixed** bulk energy density $\psi_\mathcal{B}^e$, whereas e) – h) illustrate the evolution for the **internally mixed** bulk energy density $\psi_\mathcal{B}^i$.*

shape of needles etc. will have to be further investigated. The value of the viscosity is chosen such that it guarantees convergence for the employed time step size and has no physical interpretation. Finally, the regularization length l is chosen to be both on a physically realistically small length scale and with $l \approx 3h$ also large enough to guarantee a sufficiently small discretization of the gradients in the interface region. For all simulations, we use $\boldsymbol{m}_o = \boldsymbol{m}_o^1$ as specified in (5).

10.3 Influence of Incoherence Penalty

In our first set of numerical experiments, we investigate both the influence of the incoherence penalty parameter λ as introduced in (32) as well as the influence of the choice of the bulk energy density $\psi_\mathcal{B}$ on the formation of microstructure. To this end, we carry out four simulations with identical random initial conditions $p(\boldsymbol{X}, t = 0) \in [0, 1]$: Two simulations without coherence-dependence, i.e. $\lambda = 0.0$: (i) with the externally mixed bulk energy density $\psi_\mathcal{B} = \psi_\mathcal{B}^e$, see Figure 7a–d and (ii) with the internally mixed bulk energy density $\psi_\mathcal{B} = \psi_\mathcal{B}^i$, see Figure 7e–h. Furthermore, we carry out two simulations with coherence-dependence, i.e. $\lambda = 100.0$: (iii) with the externally mixed bulk energy density $\psi_\mathcal{B} = \psi_\mathcal{B}^e$, see Figure 8a–d and (iv) with the internally mixed bulk energy density $\psi_\mathcal{B} = \psi_\mathcal{B}^i$, see Figure 8e–h. All simulations are carried out with a time step of $\Delta t = 0.001$s.

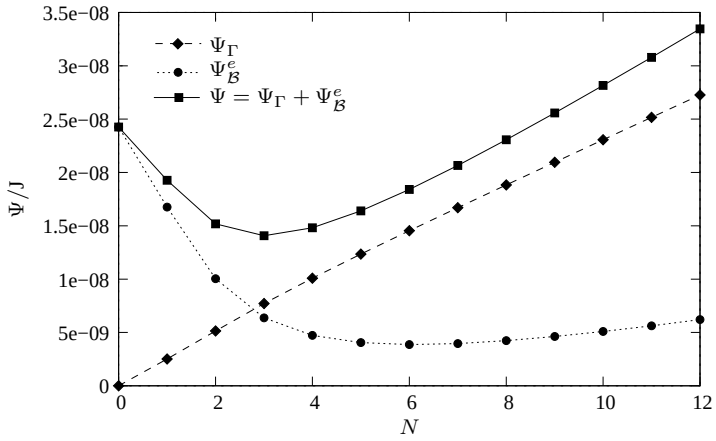

Figure 9: *Dependence of the **coherence-dependent** interface energy Ψ_Γ ($\lambda = 100.0$), the **externally mixed** bulk energy $\Psi^e_\mathcal{B}$ and the total energy $\Psi = \Psi_\Gamma + \Psi^e_\mathcal{B}$ of a body under boundary conditions (76) on the number of layers of martensitic twins N. Note that $\Psi^e_\mathcal{B} \nrightarrow 0$ for $N \to \infty$ in disagreement with Chipot and Kinderlehrer (1988).*

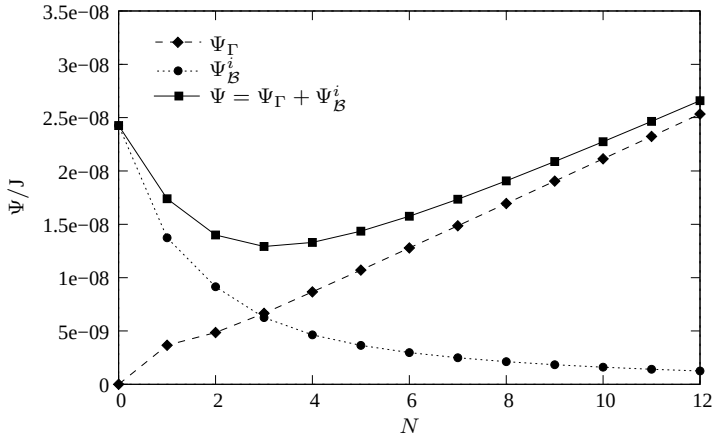

Figure 10: *Dependence of the **coherence-dependent** interface energy Ψ_Γ ($\lambda = 100.0$), the **internally mixed** bulk energy $\Psi^i_\mathcal{B}$ and the total energy $\Psi = \Psi_\Gamma + \Psi^i_\mathcal{B}$ of a body under boundary conditions (76) on the number of layers of martensitic twins N. Note that $\Psi^i_\mathcal{B} \to 0$ for $N \to \infty$ as shown by Chipot and Kinderlehrer (1988).*

As can be seen by comparing the columns of Figures 7 as well as 8, the choice of the bulk energy density $\psi_\mathcal{B}$ has no drastic influence on the resulting microstructure. The most obvious difference is the slower evolution for $\psi_\mathcal{B} = \psi^i_\mathcal{B}$ that possibly stems from the different definition of the driving force. It should be noted that in contrast to the external mixing, for the choice $\psi_\mathcal{B} = \psi^i_\mathcal{B}$, the phasefield p does not take on values outside the admissible range $[0, 1]$.

In contrast to the choice of the bulk energy, a comparison of Figures 7 and 8 shows that the value of the incoherence penalty parameter λ has a drastic influence on the resulting microstructure. A value of $\lambda = 0.0$ leads to the formation of initial microstructure that resembles the microstructure in diffusive transformations more than that of martensitic phase changes, see Figure 7. Towards the end of the simulation with $\lambda = 0.0$, the interfaces start to orient themselves towards the two solutions $\boldsymbol{m}^1_o$ and $\boldsymbol{m}^2_o$ of the twinning equation as given in 5 but do not form the characteristic laminate microstructure. On the other hand, an incoherence penalty value of $\lambda = 100.0$ leads to the initial formation of the typical needle shaped domains of the different variants that then traverse the body to form characteristic martensitic laminates with coherent interfaces, see Figure 8.

In summary, we see from the simulations that the use of a coherence-dependent interface energy is required to suitably predict the formation of martensitic laminate microstructure. The choice of the bulk energy influences the rate of evolution but seems to have no effect on the form of the resulting microstructure.

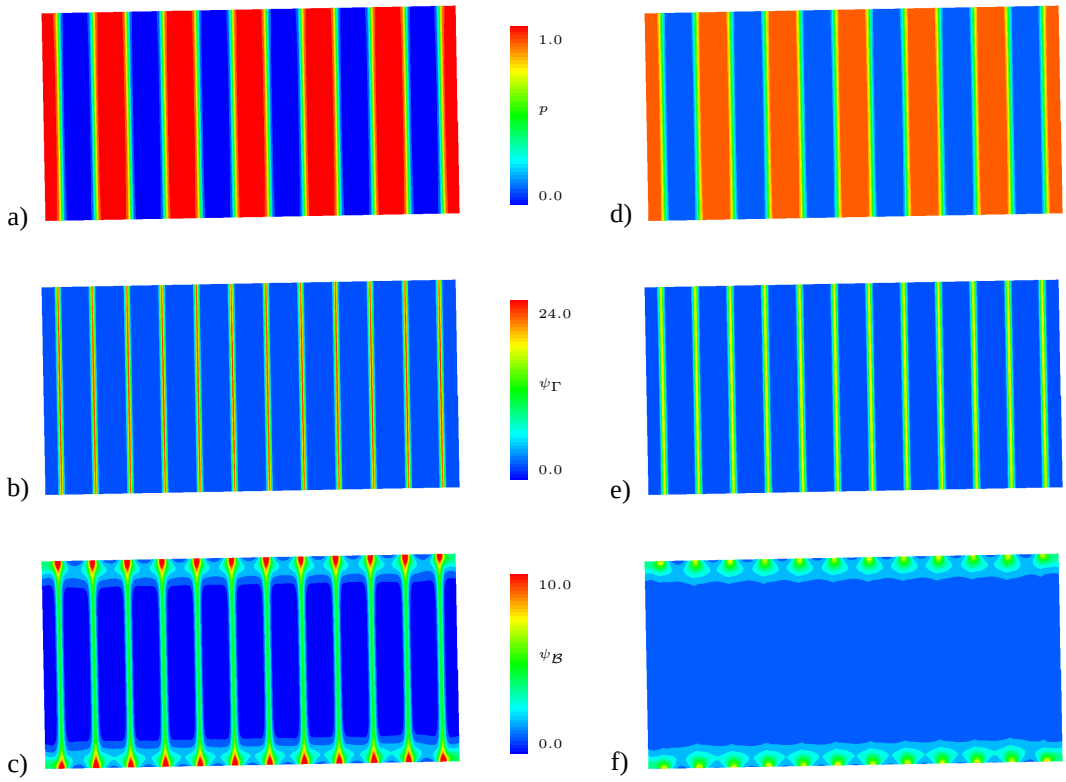

Figure 11: *Comparison of phasefield and energy density distributions for* ***externally mixed*** *(a)–c)) bulk energy* $\psi^e_\mathcal{B}$ *and* ***internally mixed*** *(d)–f)) bulk energy* $\psi^i_\mathcal{B}$*. a) and d) show the phasefield distributions* $p(\boldsymbol{x})$ *of an equilibrated initial configuration with six layers. b) and e) show the distributions of the interface energy density* $\psi_\Gamma(\boldsymbol{x})/1000\mathrm{N/m}$ *and c) and f) show the distributions of the interface energy density* $\psi_\mathcal{B}(\boldsymbol{x})/1000\mathrm{N/m}$*.*

10.4 Energetics of Laminate Length Scales

As observed in the first set of experiments, the choice of the bulk energy $\psi_\mathcal{B}$ had almost no effect on the resulting microstructure. We now want to investigate the effect of the choice of the bulk energy on the energetic modeling of the two approaches. To do so, we carry out an additional series of simulations. The idea is to identify the specific laminate length scale that minimizes the total energy Ψ of the laminate for the given sample size, and to better understand the competition between interface energy Ψ_Γ and bulk energy $\Psi_\mathcal{B}$ for differently fine laminates. To this end, we prescribe smooth representations of laminates with $N \in 0, ..., 12$ laminate pairs of thickness $M = L/N$ each as initial conditions. We compute the evolution of p with a time step of $\Delta t = 0.01$s until equilibrium is reached, and then calculate the total energy Ψ as well as the interface energy Ψ_Γ and the bulk energy $\Psi_\mathcal{B}$. We carry out this simulation both for $\psi_\mathcal{B} = \psi^e_\mathcal{B}$ and $\psi_\mathcal{B} = \psi^i_\mathcal{B}$. Figure 9 shows the resulting plot for the choice of $\psi_\mathcal{B} = \psi^e_\mathcal{B}$. As expected, Ψ_Γ linearly increases with an increasing number of interfaces, i.e. $\Psi_\Gamma \propto N$. The bulk energy $\psi_\mathcal{B}$ first decreases, but then increases again. Note that hence the bulk energy $\psi_\mathcal{B} = \psi^e_\mathcal{B}$ does not vanish for an infinitely fine laminate $N \to \infty$. This is not in agreement with the analytical results of Chipot and Kinderlehrer (1988). Figure 10 shows the resulting plots of $\Psi(N)$,$\Psi_\Gamma(N)$ and $\Psi_\mathcal{B}(N)$ for the choice $\psi_\mathcal{B} = \psi^i_\mathcal{B}$. Again, Ψ_Γ linearly increases with an increasing number of interfaces, i.e. $\Psi_\Gamma \propto N$ as expected. Furthermore, in contrast to the external mixing, the choice of $\psi_\mathcal{B} = \psi^i_\mathcal{B}$ leads to a proportionality of $\Psi_\mathcal{B} \propto 1/N$ such that $\psi^i_\mathcal{B} \to 0$ for $N \to \infty$. This is now in agreement with the analytical results of Chipot and Kinderlehrer (1988).

The reason for the inconsistent energetics of the choice $\psi_\mathcal{B} = \psi^e_\mathcal{B}$ can be understood by looking at the equilibrium distributions of bulk and interface energy density for the two approaches. Figure 11 compares the distributions of $\psi_\Gamma(\boldsymbol{x})$ and $\psi_\mathcal{B}(\boldsymbol{x})$. Obviously, the externally mixed bulk energy density $\psi^e_\mathcal{B}$ leads to artefact bulk energy contributions in the interface region. This is due to the fact that $\psi^e_\mathcal{B}$ is only zero for $\boldsymbol{F} = \boldsymbol{R}\boldsymbol{U}_1$ and $\boldsymbol{F} = \boldsymbol{R}\boldsymbol{U}_2$ for $\boldsymbol{R} \in SO(3)$ and hence does not allow any bulk energy free deformation states connecting the two minima $\boldsymbol{U}_1$ and $\boldsymbol{U}_2$. However, a bulk energy free connection of the minima is necessary to prevent bulk energy contributions in the interface region. Such a connection is facilitated by the internally mixed bulk energy density $\psi^e_\mathcal{B}$ that allows bulk energy free deformation states on the rank one connection between $\boldsymbol{U}_1$ and $\boldsymbol{U}_2$ parametrized by (42).

In summary, we see from the simulations that even though both choices of bulk energy lead to qualitatively similar microstructures, only the the choice $\psi_{\mathcal{B}} = \psi^i_{\mathcal{B}}$ allows an energetically concise modeling of two-variant martensitic shape memory alloys. This energetically concise modeling is the prerequisite for the prediction e.g. of size effects. Altogether, we thus see that a proper phasefield modeling of martensitic laminate microstructure is only possible if a coherence-dependent interface energy is used together with an internally mixed bulk energy.

11 Conclusion

In this work, we have presented a large strain phasefield model for two-variant martensitic laminate microstructure. Our model accounts for the coherence-dependence of the surface energy of twin interfaces and employs an evolution of generalized Ginzburg-Landau type. We have considered two different approaches to the modeling of bulk energy: external and internal mixing. Our considerations and simulations show that both driving forces are connected to the energy momentum tensor: the driving force resulting from external mixing is linked to the energy part and the driving force resulting from internal mixing is linked to the momentum part. Together with the coherence-dependent interface energy, both bulk energy approaches are capable of predicting the formation of martensitic laminate microstructure. However, further investigations show that in contrast to the internal mixing approach, the external mixing approach is energetically not fully concise and does not allow for the reproduction of analytical results related to the vanishing of bulk energy for infinitely fine laminates. This inconsistency is caused by the fact that the external mixing causes bulk energy contributions in the interface region.

12 Acknowledgement

The authors would like to thank the German Research Foundation (DFG) for financial support of the project within the Cluster of Excellence in Simulation Technology (EXC 310/1) at the University of Stuttgart. Furthermore, fruitful discussions with Eric Jägle are gratefully acknowledged.

References

Abeyaratne, R.; Chu, C.; James, R.: Kinetics of materials with wiggly energies: Theory and application to the evolution of twinning microstructures in a Cu-AI-Ni shape memory alloy. *Philosophical Magazine A*, 73(2), (1996), 457–497.

Abeyaratne, R.; Knowles, J.: On the driving traction acting on a surface of strain discontinuity in a continuum. *Journal of the Mechanics and Physics Solids*, 38, (1990), 345–360.

Abeyaratne, R.; Knowles, J.: *Evolution of phase transitions: A continuum theory*. Cambridge University Press, Cambridge (2006).

Alber, H.; Zhu, P.: Solutions to a model for interface motion by interface diffusion. *Proceedings of the Royal Society of Edinburgh*, 138A, (2008), 923–955.

Alberti, G.; Baldo, S.; Orlandi, G.: Variational convergence for functionals of Ginzburg-Landau type. *Indiana University Mathematics Journal*, 54, 5, (2005), 1411–1472.

Allen, S.; Cahn, J.: Microscopic theory for antiphase boundary motion and its application to antiphase domain coarsening. *Acta Metallurgica*, 27, 6, (1979), 1085–1095.

Artemev, A.; Jin, Y.; Khachaturyan, A.: Three-dimensional phase field model and simulation of cubic → tetragonal martensitic transformation in polycrystals. *Philosophical Magazine A-Physics of Condensed Matter Structure Defects and Mechanical Properties*, 82, 6, (2002), 1249–1270.

Auricchio, F.; Taylor, R.; Lubliner, J.: Shape-memory alloys: Macromodelling and numerical simulations of the superelastic behavior. *Computer Methods in Applied Mechanics and Engineering*, 146, (1997), 281–312.

Ball, J.; James, R.: Fine phase mixtures as minimizers of energy. *Archive for Rational Mechanics and Analysis*, 100, 1, (1987), 13–52.

Bertram, A.: Thermo-mechanical constitutive equations for the description of shape memory effects in alloys. *Nuclear Engineering and Design*, 74, (1982), 173–182.

Bhattacharya, K.: *Microstructure of Martensite*. Oxford University Press, Oxford (2003).

Boyd, J.; Lagoudas, D.: A thermodynamical constitutive model for shape memory materials .1. the monolithic shape memory alloy. *International Journal of Plasticity*, 12 (6), (1996), 805–842.

Chipot, M.; Kinderlehrer, D.: Equilibrium-configurations of crystals. *Archive for Rational Mechanics and Analysis*, 103, 3, (1988), 237–277.

Duerig, P.; Melton, K.; Stockel, D.; Wayman, C.: *Engineering Aspects of Shape Memory Alloys*. Butterworth-Heinemann, Boston, MA (1990).

Eshelby, J.: The Continuum Theory of Lattice Defects. vol. 3 of *Solid State Physics*, pages 79–144, Academic Press (1956).

Faran, E.; Shilo, D.: The kinetic relation for twin wall motion in NiMnGa. *Journal of the Mechanics and Physics of Solids*.

Fried, E.; Grach, G.: An order-parameter-based theory as a regularization of a sharp-interface theory for solid-solid phase transitions. *Archive for Rational Mechanics and Analysis*, 138, (1997), 355–404.

Fried, E.; Gurtin, M.: Continuum theory of thermally induced phase transitions based on an order parameter. *Physica D: Nonlinear Phenomena*, 68, (1993), 326–343.

Gurtin, M.: Generalized Ginzburg-Landau and Cahn-Hilliard equations based on a microforce balance. *Physica D*, 92, 3-4, (1996), 178–192.

Helm, D.; Haupt, P.: Shape memory behaviour: Modelling within continuum thermomechanics. *International Journal of Solids and Structures*, 40, 4, (2003), 827–849.

Hildebrand, F.; Abeyaratne, R.: An atomistic investigation of the kinetics of detwinning. *Journal of the Mechanics and Physics of Solids*, 56, (2008), 1296–1319.

Hou, T.; Rosakis, P.; LeFloch, P.: A level-set approach to the computation of twinning and phase-transition dynamics. *Journal of Computational Physics*, 150, (1999), 302–321.

Jacobs, A.; Curnoe, S.; Desai, R.: Simulations of cubic-tetragonal ferroelastics. *Physical Review B*, 68, 22.

James, R.: Finite deformation by mechanical twinning. *Archive for Rational Mechanics and Analysis*, 77, (1981), 143–176.

Ji, H.; Chopp, D.; Dolbow, J.: A hybrid extended finite element/level set method for modeling phase transformations. *International Journal for Numerical Methods in Engineering*, 54, (2002), 1209–1233.

Levitas, V.; Lee, D.; Preston, D.: Interface propagation and microstructure evolution in phase field models of stress-induced martensitic phase transformations. *International Journal of Plasticity*, 26, 3, (2010), 395–422.

Levitas, V.; Levin, V.; Zingerman, K.; Freiman, E.: Displacive phase transitions at large strains: Phase-field theory and simulations. *Physical Review Letters*, 103, (2009), 025702.

Merkle, C.; Rohde, C.: Computation of dynamical phase transitions in solids. *Applied Numerical Mathematics*, 56, (2006), 1450–1463.

Miehe, C.: A multi-field incremental variational framework for gradient-extended standard dissipative solids. *Journal of the Mechanics and Physics of Solids*, 59, (2010), 898–923.

Miehe, C.; Welschinger, F.; Hofacker, M.: Thermodynamically consistent phase-field models of fracture: Variational principles and multi-field fe implementations. *International Journal for Numerical Methods in Engineering*, 83, (2010), 1273–1311.

Modica, L.: The gradient theory of phase transitions and the minimal interface criterion. *Annales de l'Institut Henri Poincare - Analyses Non Lineaire*, 4, (1987), 487–512.

Murr, L.: *Interfacial Phenomena in Metals and Alloys*. Addison-Wesley (1975).

Ostsuka, K.; Shimizu, K.: Morphology and crystallography of thermoelastic Cu-Al-Ni martensite analyzed by the phenomenological theory. *Transactions of the Japan Institute of Metals*, 15(2), (1974), 103–108.

Porter, D.; Easterling, K.: *Phase Transformations in Metals and Alloys*. Chapman & Hall (1992).

Qidwai, M.; Lagoudas, D.: Numerical implementation of a shape memory alloy thermomechanical constitutive model using return mapping algorithm. *International Journal for Numerical Methods in Engineering*, 47, (2000), 1123–1168.

Rasmussen, K.; Saxena, A.; Bishop, A.; Albers, R.; Shenoy, S.: Three-dimensional elastic compatibility and varieties of twins in martensites. *Physical Review Letters*, 87(5), (2001), 055704.

Address: Institute of Applied Mechanics, University of Stuttgart, Pfaffenwaldring 7, 70550 Stuttgart
email: `felix.hildebrand@mechbau.uni-stuttgart.de`